



A novel thermo-geometrical model for accurate keyhole porosity prediction in Laser Powder-Bed Fusion

Emanuele Vaglio¹ · Giovanni Totis¹ · Alex Lanzutti¹ · Lorenzo Fedrizzi¹ · Marco Sortino¹

Received: 16 June 2022 / Accepted: 7 April 2023
© The Author(s) 2023

Abstract

When performing Laser Powder-Bed Fusion, undesired physical phenomena, such as balling, preballing and keyhole, must be avoided in order to achieve high-quality products. To date, keyhole-free process parameters can be identified either using demanding empirical methods or complex numerical simulations, while only a few analytical models can be found in literature for this purpose. In this work, state-of-the-art analytical models for predicting keyhole porosity were summarized and proved to be rather inaccurate because they are only based on thermodynamic principles, whereas they neglect the geometry and both the kinetics and kinematics of the keyhole cavity, which do also influence cavity collapse and porosity formation. Here an innovative physics-based semi-analytical model for predicting the formation of keyhole-related porosities was conceived, in which both thermodynamic and geometrical factors are taken into account. The proposed model was validated by performing single tracks experiments on Ti6Al4V according to a full factorial DoE on laser power and scanning speed. Produced samples were cross-sectioned and analyzed to evaluate keyhole porosity formation. The comparison between experimental data and model predictions confirmed the higher accuracy of the new model with respect to state of the art models. Besides improving the understanding of the keyhole phenomenon, the proposed model may provide a novel, effective and simple tool for fast process parameter optimization in industry.

Keywords Laser Powder-Bed Fusion · Keyhole · Porosity · Predictive model · Process parameters optimization

List of symbols

A	Absorptivity
A_{bal}	Balanced accuracy of predictive models
B	Material constant in $v_{cr,g}$
c	Specific heat
D	Thermal diffusivity
d_s	Laser spot diameter
E^*	Dimensionless heat input
H	Enthalpy
h_d	Hatch distance
h_s	Enthalpy at melting
H_v	Enthalpy at vaporization
k	Thermal conductivity
L_m	Latent heat of melting
L_v	Latent heat of vaporization

N_{ff}	Number of pore-free cases correctly classified by a model
$N_{f,tot}$	Number of pore-free cases experimentally observed
N_{kk}	Number of pore-affected cases correctly classified by a model
$N_{k,tot}$	Number of pore-affected cases experimentally observed
P	Laser power
T_0	Ambient temperature
T_b	Boiling temperature
t_{clo}	Closing time
$t_{cr,t}$	Critical time
T_v^{eff}	Effective vaporization temperature
t_{int}	Laser–material interaction time
t_l	Layer thickness
T_m	Melting temperature
T_p^*	Dimensionless peak temperature
v	Scanning speed
v^*	Dimensionless scanning speed
v_{clo}	Closing speed
$v_{cr,g}$	Critical scanning speed related to cavity geometry

✉ Emanuele Vaglio
emanuele.vaglio@uniud.it

¹ Polytechnical Department of Engineering and Architecture, University of Udine, Via delle Scienze 206, 33100 Udine, Italy

$v_{cr,t}$	Critical scanning speed related to thermodynamics
z^*	Dimensionless depth
ρ	Density

1 Introduction

Laser Powder-Bed Fusion (LPBF) is an increasingly widespread technology for producing cutting-edge products in strategic sectors. It promotes significant technological progress and competitive advantages to the users.

Nevertheless, the possibility of making finished products using LPBF depends on the selection of suitable process parameters. According to Grasso et al. [1], there are 6 classes of defects that may affect LPBF products:

1. porosity;
2. residual stresses, cracking and delamination;
3. balling;
4. geometric defects and dimensional accuracy;
5. surface defects;
6. microstructural inhomogeneities and impurities.

Among them, porosity plays a key role because it may dramatically affect the mechanical behavior of the processed material [2].

Porosity can form due to lack of fusion between tracks and layers [3] or due to the inclusion of gas and other volatile elements in the molten pool. According to Hojjatzadeh et al. [4], there are 6 pore formation mechanisms of the latter type: pore transfer from feedstock powder; keyhole; surface fluctuation due to droplet impact; shallow cavity collapse; pore induction by cracks; vaporization of volatile substances around the melting boundary. Among them, keyhole phenomenon is the most relevant in terms of both frequency and impact on the material properties. It consists in the formation of a deep cavity inside the molten pool, and it typically causes the formation of large and spherical pores, which clearly differ from the irregular ones deriving from other phenomena [5].

The keyhole phenomenon was extensively investigated over the last 20 years. The most relevant research work on this topic is summarized in Table 1. According to Ki et al. [6], it mainly depends on the thermocapillary force, the recoil pressure, the surface tension and the increase in absorptivity due to the multiple reflections of the laser rays inside the cavity. However, the predominant role is assumed by the recoil pressure [7], presumably due to the effect it has on temperature distribution [8].

The keyhole cavity behavior is determined by the competitive action of recoil pressure and surface tension [9], which results in a cyclical evolution [10] causing the molten metal to spill from the back cavity wall towards

the front one [11]. As a result, the cavity collapses and a pore is possibly formed (Fig. 1a). However, Fabbro [12] experimentally observed that the conventional description of the keyhole mechanism based on thermodynamic principles is valid only when the speed of the laser beam is below a certain threshold, which is function of the process conditions, and that the keyhole cavity behavior distinctly varies when it is exceeded. At sufficiently high scanning speeds, other physical phenomena play indeed a significant role on the formation of keyhole-related pores inside the 3D printed component. In the last years, several authors studied these phenomena, as it will be recalled in the next section, by also proposing different methodologies for keyhole prediction in the medium-high scanning speed regime. Nevertheless, a simple and effective tool for keyhole prediction under these conditions is still missing.

In this work, a new semi-analytical model for the keyhole porosity prediction is presented. Compared to the state-of-the-art models,

- it derives the conventional thermodynamic threshold used to predict the keyhole porosity formation in an innovative way. Compared to conventional models, it is expected to provide more accurate results while reducing the number of factors and levels to be tested for the experimental identification of the model coefficients;
- it introduces an innovative and more accurate criterion for the keyhole porosity prediction that accounts for the kinematics phenomena resulting from the increase in scanning speed.

The latter criterion will be based on a geometrical–kinematic analysis of keyhole cavity evolution.

The obtained model will ultimately depend on the considered powder material, on the laser focus diameter, on the laser power and on the scanning speed, by means of simple relations that can be determined from a limited number of experimental tests.

The model was experimentally validated through the analysis of Ti6Al4V single tracks, and the results indicated its greater accuracy in comparison to other available models. Also, this methodology provides a novel, effective and simple tool that may contribute to a fast process parameter optimization in industry.

2 State of the art on keyhole prediction

Dynamics of keyhole formation and collapse do strongly depend on the scanning speed. Different keyhole mechanisms arise at low and medium-high scanning speeds, as it was experimentally confirmed by several authors in the last years. In a recent literature review, Teng et al. [31] pointed

Table 1 Summary of the most relevant research works studying the keyhole phenomenon

Ref.	Method	Mat.	P [W]	v [mm/s]	d_s [μm]	t_l [μm]	h_d [μm]	Sample
[6]	Sim.	Mild steel	4000	25.4	500	0	–	ST
[7]	Sim., Exp.	Mild steel	2400–4000	25.4–42.3	500	0	–	ST
[8]	Sim., Exp.	AISI 316L	200	300–2500	70	30	65	ST, 3D
[9]	Sim., Exp.	Mild steel	9000	0	300	0	–	SN
[10]	Exp.	Ti6Al4V	200	100	50	100	–	ST
[11]	Sim.	Mild steel	100–2000	0	300	0	–	SN
[12]	Exp., An.	AISI 304 (Mild steel)	2500–4000 (4000–6300)	16.7–833.3 (16.6–250)	450–600 (125–1000)	0 (0)	–	ST (ST)
[13]	Sim., Exp.	AA5182	2500–6000	50–200	600	0	–	ST
[14]	Sim., Exp.	AA5083-O	6000	33.3–133.3	72	0	–	ST
[15]	Exp.	AISI 304	1000–5000	16.7–166.7	400	0	–	ST
[16]	Exp.	AISI 316L	140–300	150–1500	100–200	50	60–240	ST, 3D
[17]	Exp.	Ti6Al4V	16–195	50–1200	n.a	30	–	ST
[18]	Exp., An.	AISI 316L	100–500	100–2500	55	75	–	ST
[19]	Exp.	AlSi10Mg MS300	200–375 (80–180)	666.6–3200 (200–1000)	70 (100–110)	30 (30–45)	80 (100–105)	3D (3D)
[20]	Exp., An.	AISI 304 (Tantalum) (Ti6Al4V) (AISI 304L) (Vanadium)	300–2000 (1900) (615–1400) (664–1980) (664–1980)	16.7–50 (0.85–12.7) (16.9) (6.4–19.1) (25.4)	320–960 (300) (300) (300) (300)	(0) (0) (0) (0) (0)	– (–) (–) (–) (–)	ST (ST) (ST) (ST) (ST)
[21]	Sim., Exp., An.	AISI 316L	[0–400]	[0–4000]	52–130	50	–	ST
[22]	Exp., An.	Ti6Al4V	200–500	100–1000	n.a	20–60	60–140	ST, 3D
[23]	Sim., Exp., An.	Inconel 718 (AISI 316L) (Ti6Al4V)	200–400 (25–400) (100–200)	300–2000 (20–1800) (200–1100)	100 (54–70) (n.a.)	40–60 (0–400) (30)	80 (124) (100)	ST, 3D (ST, 3D) (3D)
[24]	Exp., An.	Ti6Al4V AlSi10Mg (Ti6Al4V) (AISI 316L)	150–300 150–400 (50–400) (150–400)	733–1363 500–786 (200–1600) (500–1800)	70 70–200 (54–100) (54)	30 30–35 (30–50) (30)	– – (–) (–)	ST ST (ST) (ST)
[25]	Exp.	AA5182 AA5754	2760 2760	105.8 63.5	n.a. n.a.	0 0	–	ST ST
[26]	Exp.	Ti6Al4V	104–520	0–1500	95–140	0–n.a	–	SN, ST
[27]	Sim., An.	AISI 304L Mild steel	7000 10000	0–120 [50–500]	350 1000	0 0	–	SN, ST ST
[28]	Sim., An.	Mild steel	2000–5000	[10–160]	1000	0	–	ST
[29]	Exp.	AA5083 AISI 304 AISI 316 AA5182	[4000–10000] 5000 [3500–4500] 2500–5000	0–150 25 0 25	[700] [700] [700] [700]	0 0 0 0	–	SN SN SN SN
[30]	Sim., An.	Steel	3000	33–600	280	0	–	ST

Hatch distances refers exclusively to 3D samples

Sim. simulation, *Exp.* experimental, *An.* Analytical, *SN* stationary, *ST* single tracks, *3D* 3D samples, [] not explicitly specified, () literature data from other sources, – not applicable, *n.a.* not available

out the increasing tendency to form pores at low scanning speeds. Lin et al. [13] experimentally showed that for combinations of medium to high laser power and sufficiently high scanning speeds the cavity became wider, fluctuations were reduced, and porosity was practically absent. The same results were experimentally and numerically obtained also by Huang et al. [14], who further emphasized that bubbles

resulting from keyhole collapse may escape more easily from the molten pool at high scanning speeds due to the lower solidification rate. Miyagi et al. [15] showed by in situ X-ray imaging that with increasing scanning speed the cavity depth decreased while its length and inclination increased.

When a deep keyhole cavity is formed under low scanning speed conditions it certainly collapses into a pore

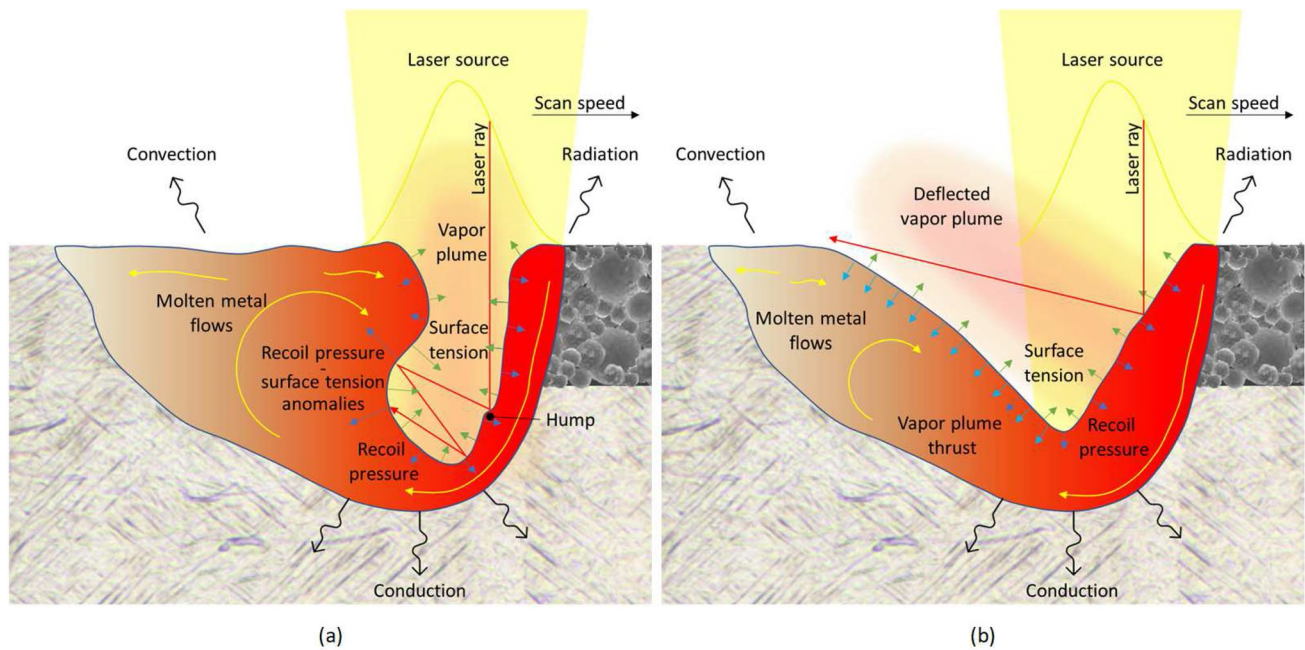


Fig. 1 Representation of the keyhole phenomenon based on the most widely accepted knowledge in literature. Dark blue arrows represent the recoil pressure, light blue arrows the vapor plume thrust, green arrows the surface tension, red arrows the laser rays and yellow arrows the molten metal flows. **a** When a deep keyhole cavity is formed under low scanning speed conditions, humps on the front wall deflect the laser rays toward the rear wall, the energy absorption dramatically increases, and local anomalies in the intensity of recoil

pressure and surface tension occur. The molten metal spills from the back cavity wall towards the front causing the cavity collapse that possibly results in the formation of a pore. **b** When the scanning speed increases, the formation of humps is prevented and the keyhole front wall progressively tilts forward causing the deviation of the plasma plume towards the keyhole rear wall, which is pushed backwards

(Fig. 1a). This occurs under the predominant effect of the recoil pressure that drives the laser penetration into the processed substrate. The recoil pressure is in turn triggered by metal vaporization which purely depends on thermodynamics since it only requires heating the material to its vaporization temperature. Consequently, in this condition the keyhole phenomenon is dominated by thermodynamics. Several models for keyhole prediction were developed in the last years that were based on purely thermodynamic arguments, as illustrated in Table 2.

The energy density is the most common quantity used to define the transition between conduction (keyhole-free) and keyhole mode. Various authors defined it in different intuitive ways, including the Linear Energy Density (LED) [16, 17] and the Volumetric Energy Density (VED) expressed in basic [18] or advanced [19] form. However, the concept is similar and in all the cases the critical threshold can only be obtained experimentally. As a consequence, this approach is of limited interest and will not be further considered in this paper.

Other common criteria for keyhole prediction are based on normalized thermodynamic quantities, such as enthalpy, evaporation energy or temperature (Table 2). However, in most cases, they refer to penetration depth

and not directly to porosity, which is the actual defect to be avoided. These two effects do not coincide, since deep keyholes not resulting in pores are possible [25].

Recently, Cunningham et al. [26] investigated the laser melting in steady conditions (i.e. with scanning speed equal to zero) through ultrahigh-speed synchrotron X-ray imaging. According to their findings, during keyhole formation the penetration rate change twice: a first transition occurs simultaneously with the onset of fluctuations and causes a rapid increase in the cavity aspect ratio, while a second transition occurs when the cavity aspect ratio becomes close to about 0.5, and consists in a reduction of the penetration rate. This work will be considered as the starting point to develop the first part of the model proposed here.

When compared to real experimental data, the above models tend to fail in the medium-high speed regime.

At medium-high scanning speeds the shape of the keyhole rear wall changes when compared to that observed in the low scanning speed regime, thus suggesting that keyhole formation and collapse are influenced by other factors.

Firstly, the local anomalies in the intensity of recoil pressure and surface tension that are typically caused by

Table 2 Analytical models predicting the transition between conduction and keyhole mode

Ref.	Class	Equation
[20]	Normalized enthalpy	$\frac{\Delta H}{h_s} = \frac{AP}{kT_m \sqrt{\frac{\pi v d_s^3}{D}}} = \frac{H_v}{h_s} \approx 10$ (1)
[21]	Normalized enthalpy	$\frac{\Delta H}{h_s} = \frac{AP}{kT_m \sqrt{\frac{\pi v d_s^3}{D}}} = \frac{\pi T_b}{T_m} \approx 5.12$ (2)
[22]	Normalized enthalpy	$\frac{\Delta H}{h_s} = \frac{0.865APD}{kT_m \sqrt{\pi v t_s d_s}} = \frac{\pi T_b}{T_m} \approx 5.12$ (3)
[23]	Adimensional energy density	$\eta_v = \frac{AP}{h_s t_s v \rho c (T_v^{eff} - T_0)} = 0.838$ (4)
[24]	Adimensional peak temperature	$\begin{cases} T_p^* = \frac{3}{2\sqrt{2\pi} e^{0.75}} \frac{E^*}{v^*} \frac{1}{(0.8+z_0^*)^2} = 1.75 \\ z_0^* = \sqrt{\frac{3\sqrt{\pi}}{2\sqrt{2} e^{0.75}} \frac{1}{v^* \tan^{-1}(\sqrt{8/v^*})}} \end{cases}$ (5)

localized heating resulting from multiple reflections of rays inside the cavity [27] cease to occur (Fig. 1b). Such anomalies can affect not only the front wall, where they may cause the formation of humps, but also the rear wall, where the rays deflected by the humps formed on the opposite border may induce a thrust that tends to widen the cavity (Fig. 1a). This mechanism was analytically, numerically and experimentally described in [7, 28] and [29], respectively, and it plays a central role in the keyhole evolution since it is a primary cause of the cavity collapse. Such phenomenon can be ultimately related to the scanning speed. Indeed, Matsunawa et al. [30] showed that humps form periodically with an increasing frequency as the scanning speed increases, up to a maximum value above which the whole wall moves slower than the laser beam. Above this limit, humps formation is prevented and the corresponding instability mechanism is not activated.

Secondly, the keyhole front wall progressively tilts forward by increasing the scanning speed. This causes the deviation of the plasma plume, which is perpendicular to it [12]. At sufficiently high scanning speeds, the deflected plume is directed towards the keyhole rear wall, which is therefore pushed backwards. As a consequence, the angle between the keyhole walls increases [28] and elongated cavities are obtained, thus preventing the formation of pores (Fig. 1b).

In short, at medium-high scanning speeds, keyhole genesis and collapse are dominated by physical phenomena that cannot be explained through pure thermodynamic arguments.

In this work, keyhole prediction at medium-high scanning speeds will be based on simple geometric and kinematic principles, as it will be showed in the next section.

3 A new model for keyhole porosity prediction

In the proposed model, two conditions concur for the keyhole development. As conventionally assumed, the first condition is met when the laser beam penetration into the base material is deep enough, while the second condition is met when the shape of the cavity is compatible with the abrupt collapse that is responsible for pores formation.

3.1 Laser–material interaction time condition

According to the work of Cunningham et al. [26] recalled in the previous section, the keyhole depth growth rate changes two times during laser exposure. The first transition consists in a sudden growth rate increase that causes the depth at least to double in a few microseconds. The second consists instead in a reduction of the depth growth rate associated to the occurrence of fluctuations. According to this, it can be inferred that deep keyhole cavities only form if the laser action lasts long enough for the first transition to occur.

By processing literature data, it can be obtained that the critical time $t_{cr,t}$ necessary for the first transition to occur can be expressed as a function of laser power P , laser spot diameter d_s and powder material properties (simply denoted $mat.$), as follows

$$t_{cr,t} = t_{cr,t}(P, d_s, mat.) \tag{6}$$

In this work, a simple model of the critical time for the Ti6Al4V alloy processed under stationary conditions was conceived for the first time by performing numerical regression in natural and logarithmic scales on the largest homogeneous set of data extracted from [26]. Fig. 2 shows the best model found by means of the stepwise regression algorithm, which has the form

$$t_{cr,t} = \gamma P^\delta d_s^\epsilon = 2.026 \cdot 10^{13} P^{-3.823} d_s^{5.836} \quad (7)$$

where P is expressed in [W], d_s is in [mm] and $t_{cr,t}$ is in [ms]. Model coefficients γ , δ and ϵ may in general depend on the considered powder material and can be experimentally estimated through stationary laser exposure by varying the laser power, the laser spot diameter and the exposure time according to a minimal factorial design. Suitable test configurations are material-independent since the data obtained are only required for numerical regression. Rather, it is recommended to explore the entire admissible ranges of parameters, which for the LPBF are reasonably narrow and typically limited to $50 \text{ W} < P < 400 \text{ W}$, $30 \mu\text{m} < d_s < 500 \mu\text{m}$ and $0.012 \text{ ms} < t < 2 \text{ ms}$. By so doing, the reliability and benefits of the proposed approach would be maximized.

In the considered case study, the squared linear correlation coefficient between the measured and the numerically predicted values of $t_{cr,t}$ was $R^2 = 0.95$.

In stationary conditions the keyhole regime is triggered if the exposure time is $t > t_{cr,t}$. In Laser Powder-Bed Fusion, the laser beam is not static, but it moves along the scanning path at a certain speed. In this case, it can be assumed that the laser–material interaction time coincides with the time interval required by the beam to travel a distance equal to its

diameter, and it should be longer than the critical time $t_{cr,t}$ for enabling keyhole onset, i.e.

$$t_{int} = \frac{d_s}{v} > t_{cr,t} \quad (8)$$

This simply yields

$$v < \frac{d_s}{t_{cr,t}} = \frac{d_s^{1-\epsilon}}{\gamma P^\delta} = v_{cr,t}(P, d_s) \quad (9)$$

where $v_{cr,t}$ is the critical, maximum scanning speed – expressed as a function of laser spot diameter and laser power – satisfying the thermodynamic conditions for keyhole formation.

In Fig. 3, the curves obtained from Eq. 9 are overlaid to the maps reporting the vapor depression morphology when solid Ti6Al4V is exposed by a moving laser beam [26]. Dashed lines are also showed, which were determined from the geometrical inspection of cavity morphology. By construction, the proposed model should approximately represent the occurrence of the first transition, which was denoted by a dashed blue line. The correspondence is in general satisfactory and very good for the smaller laser spot, presumably because in such a case the laser energy distribution is narrower, implying a well-defined entry and exit of the beam from the instantaneously processed region demarcated by the laser beam diameter. Conversely, larger laser beams have low intensity tails that contribute to the interaction time despite being actually ineffective in sustaining the cavity.

As a final remark, it is worth noting that the dataset used here was derived by processing a solid surface, not a layer of powder as would happen in real process conditions. However, [26] noticed that the presence of metal powder only results in a second-order effect when the keyhole depth is analyzed.

3.2 The geometrical condition

The curve derived in the previous section applies only at low scanning speeds, that is when thermodynamics are dominant. At medium-high scanning speeds, the cavity shape changes considerably and other factors become more important. Under these circumstances, the cavity elongation along the scanning speed direction may prevent the rear section from joining the front wall.

Actually, the formation of elongated cavities cannot be simply explained by the deviation of the plasma plume resulting from the front wall inclination. Indeed, the X-ray images in Fig. 3 show only small differences in the front wall inclination between the different cases. To discuss the longitudinal development of the cavity, it is useful to recall the closing speed v_{clo} introduced by [27], which is the velocity at which the fluid behind the cavity moves along the

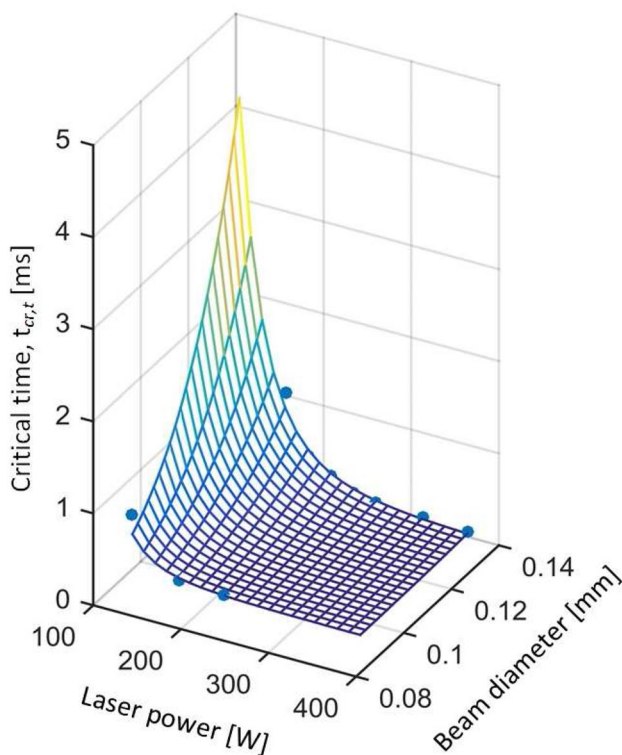
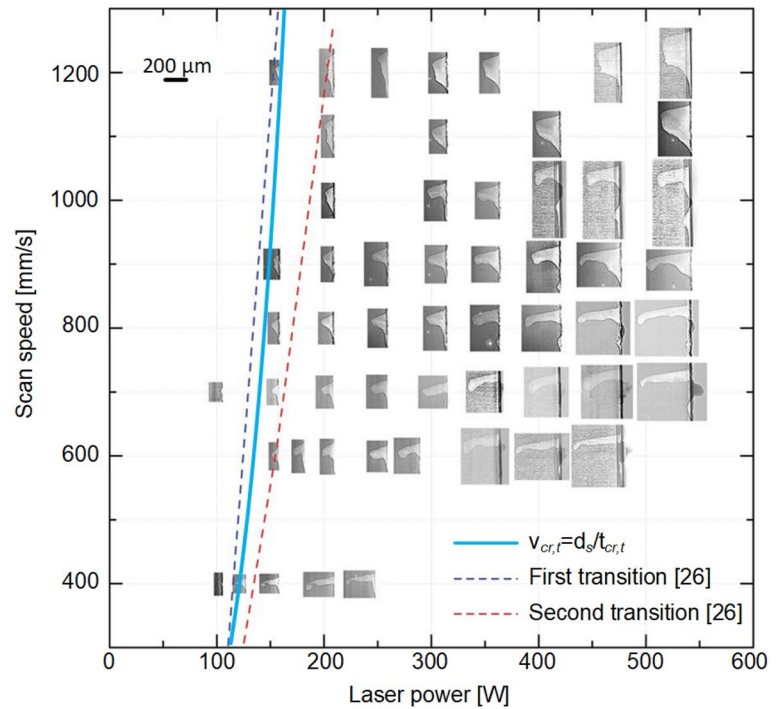
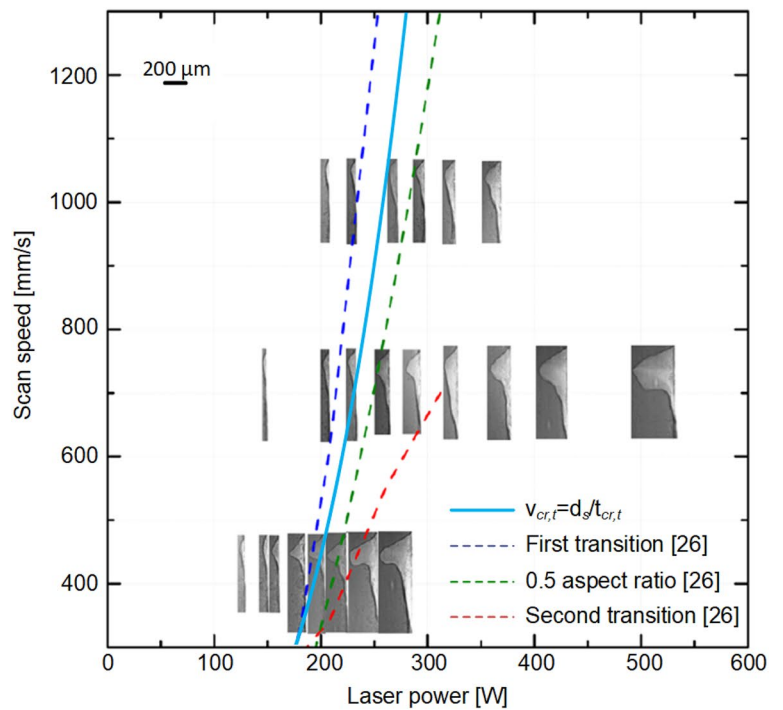


Fig. 2 Critical time required for the first transition to occur: measured points (blue dots) [26] and interpolating model (colored surface)

Fig. 3 Keyhole prediction based on interaction time (Eq. (9)) compared to vapor depression morphology when solid Ti6Al4V is exposed under non-stationary condition: **a** $d_s = 95 \mu\text{m}$, **b** $d_s = 140 \mu\text{m}$ [26]



(a)



(b)

scanning direction. According to the scheme in Fig. 4, it can be argued that narrow keyholes are only possible if the scanning speed v is lower than the maximum possible closing speed $v_{clo,max}$, i.e.

$$v \leq v_{clo,max} = v_{cr,g} \tag{10}$$

where $v_{cr,g}$ denotes the critical, maximum scanning speed satisfying the geometrical conditions for keyhole formation. Indeed, when $v \leq v_{clo,max}$, the effective closing speed v_{clo} can adjust itself to match the scanning speed within an

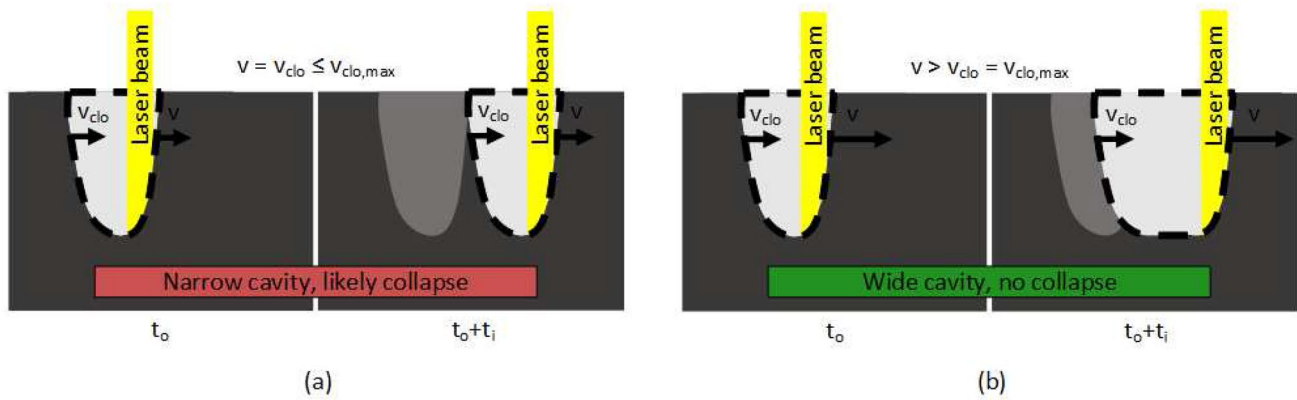


Fig. 4 Vapor depression lengthening mechanism based on the comparison between the scanning speed v and the closing speed v_{clo} . **a** When the scanning speed v is lower than the closing speed v_{clo} the

equilibrium framework resulting in the formation of narrow cavities. Conversely, when $v > v_{clo,max}$, the front wall moves away from the back wall and wide, more stable cavities are formed.

The closing speed v_{clo} depends on the surface tension, on the recoil pressure and on the molten metal density [27]. In turn, they imply the following dependencies.

- The surface tension depends on the processed material and on the spatial thermal gradients [32]. The spatial thermal gradients are in turn a direct consequence of the molten pool shape [33], which regulates heat conduction, and of the evaporation temperature present at the surface of the molten pool, that is a characteristic of the considered material.
- The recoil pressure depends on the processed material and on the temperature of the vapor flowing away from the cavity and forming the vapor plume, which is further influenced by the laser beam diameter and by the shape of both the molten pool and the keyhole, which control light absorption and heat conduction.
- The molten metal density is clearly an intrinsic material property that may further depend on temperature. As already mentioned, the temperature may be assumed close to the evaporation temperature, which is again a constant material property.

In conclusion, the closing speed v_{clo} can be assumed as a function of the processed material, of the laser beam diameter and of the molten pool shape. The latter is related here to heat conduction and light absorption, which were observed respectively in [33] and in [34] to strongly depend on the beam diameter. Consequently, the following ultimate relation holds:

cavity may abruptly collapse forming a pore. **b** When the scanning speed v is higher than the closing speed v_{clo} , the cavity elongates preventing the abrupt collapse and the formation of pores

$$v_{cr,g} = v_{clo,max} = f(mat., d_s) \quad (11)$$

This is the second key assumption adopted in this work to identify the keyhole regime. Accordingly, here the following simple model is proposed:

$$v_{cr,g} = B \cdot d_s \quad (12)$$

where B is a constant which depends on the processed material and it is equivalent to the reciprocal of a time. More precisely,

$$\frac{1}{B} = \frac{d_s}{v_{cr,g}} = \frac{d_s}{v_{clo}} = t_{clo} \quad (13)$$

can be interpreted as the “closing time” required for the vapor depression to be filled with molten metal.

In order to estimate this parameter when the processed material is Ti6Al4V, the X-rays images provided in [26] were used, where the boundaries separating short from long vapor depressions can be easily detected.

Specifically, the critical speed $v_{cr,g}$ was approximately 1050 mm/s when d_s was 95 μm , thus yielding

$$t_{clo} \approx \frac{d_{s,1}}{v_{cr,g,1}} = \frac{0.095}{1050} = 0.091 \text{ ms} \quad (14)$$

while it was about 1150 mm/s when d_s was 115 μm , yielding a similar estimate

$$t_{clo} \approx \frac{d_{s,1}}{v_{cr,g,1}} = \frac{0.115}{1150} = 0.100 \text{ ms} \quad (15)$$

For the sake of simplicity the closing time for this material was eventually approximated by the arithmetic average of the above estimates, i.e. $t_{clo} \approx 0.096$ ms.

It is worth noting that adopting a threshold scanning speed separating the conduction mode from the keyhole mode is also consistent with the experimental data obtained by Tenbrock et al. [16] for stainless steel and by Wang et al. [23] for Inconel 718, provided that the closing time is calibrated for each material.

3.3 Model calibration through experimental data

The developed model can be easily identified in practice by indirectly estimating the critical time $t_{cr,t}$ as a function of the laser power and beam diameter, and the closing time t_{clo} .

The critical time can be determined by carrying out the following steps:

1. perform laser exposures under stationary conditions by varying the laser beam power, the laser spot diameter and the exposure time according to a minimal design of experiments;
2. inspect the cross sections of the produced samples in order to measure the molten depth and identify when the penetration rate transition occurs, for any fixed laser beam power and laser spot diameter;
3. estimate unknown model coefficients by linear regression.

Second, the closing time can be determined as follows:

1. detect keyhole pores in single tracks produced by varying the laser power, scanning speed and spot diameter according again to a minimal full or fractional design;
2. inspect tracks cross sections in order to identify the scanning speed corresponding to the transition from keyhole-free to keyhole regimes;
3. estimate the average closing time.

In any case, some experimental work is necessary, but it requires less effort when compared to traditional models.

4 Experimental validation

The proposed model was experimentally validated by analyzing the presence of keyhole pores in single scanned tracks. The experiments were performed on Ti6Al4V alloy, whose chemical composition is reported in Table 3.

The powder morphology, shape and dimensional distribution were analyzed by Scanning Electron Microscope (Zeiss

Evo 40 equipped with EDXS INCA X-sight). As shown in Fig. 5, the particles were spherical and had a diameter ranging between about 6.5 μm and 70 μm with a slight negative skewness.

The specimens were manufactured on a commercial Concept Laser M2 Cusing machine equipped with a 400 W single-mode ytterbium-doped fiber laser. Specifically, 160 single tracks were produced according to a full factorial design of experiment by varying laser power on 8 levels from 50 to 400 W (i.e. the entire range permitted by the machine) by discrete increments of 50 W, scanning speed on 10 levels from 250 to 2500 mm/s (i.e. the entire technologically significant range) by discrete increments of 250 mm/s and by also performing two replicates to enhance the reliability of the results (one replicate is illustrated in Fig. 6). In order to test the validity of the proposed model in a rather extreme configuration, single tracks were produced in a particularly critical condition, that is when a small laser spot ($d_s = 50 \mu\text{m}$) is applied [33]. Correspondingly, a small layer thickness ($t_l = 25 \mu\text{m}$) was also set.

Each track was 10 mm long, and they were scanned in groups of ten on the top surface of basic structures previously built in the same job for reproducing highly realistic operating conditions and streamline the examination procedure. The basic structures were rectangular blocks $33 \times 16 \times 5 \text{ mm}^3$ in size that were produced using the the following process parameters: laser power $P = 225 \text{ W}$, scanning speed $v = 1300 \text{ mm/s}$, laser spot diameter $d_s = 155 \mu\text{m}$, hatch distance $h_d = 105 \mu\text{m}$, layer thickness $t_l = 25 \mu\text{m}$. The exposure was executed dividing each layer into $5 \times 5 \text{ mm}^2$ squares that were bi-directionally scanned along mutually perpendicular directions.

The produced specimens were sectioned, embedded in epoxy resin, ground and polished to obtain a mirror like surface. The last polishing step was done using the colloidal silica. Subsequently, the specimens were etched using Kroll reagent for 1 minute and analyzed by optical microscope to evaluate the tracks shape and the presence of keyhole porosity. Three sections were cross sectioned and then inspected for each track. The process parameters combinations was classified as affected by keyhole in case one or more pores were found. Only when no pores at all were detected, the experimental point was classified as free of keyhole phenomena. By so doing, it was possible to assess the absence or presence of keyhole pores with a sufficient level of confidence. According to the data reported by Shrestha et al. [17], the expected probability of misclassifying a keyhole affected sample was indeed less than 4%. At the same time, the probability of misclassifying a keyhole free sample was null except at the transition

Table 3 Chemical composition of the powder used for the experiments

Chemical element	Al	V	Fe	O	C	N	H	Ti
Ti6Al4V (% weight)	6.5	4.14	0.18	0.1	0.008	0.007	0.003	89.06

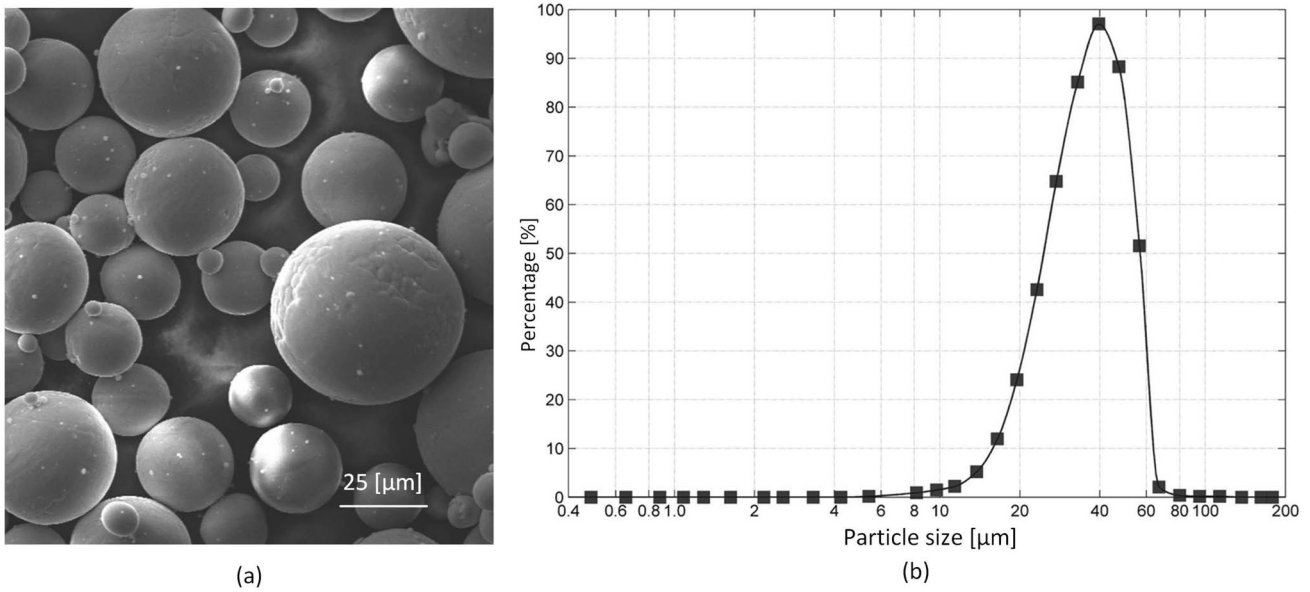


Fig. 5 Characterization of Ti6Al4V powders used for the experiments: **a** morphology inspected by SEM and **b** particle size distribution

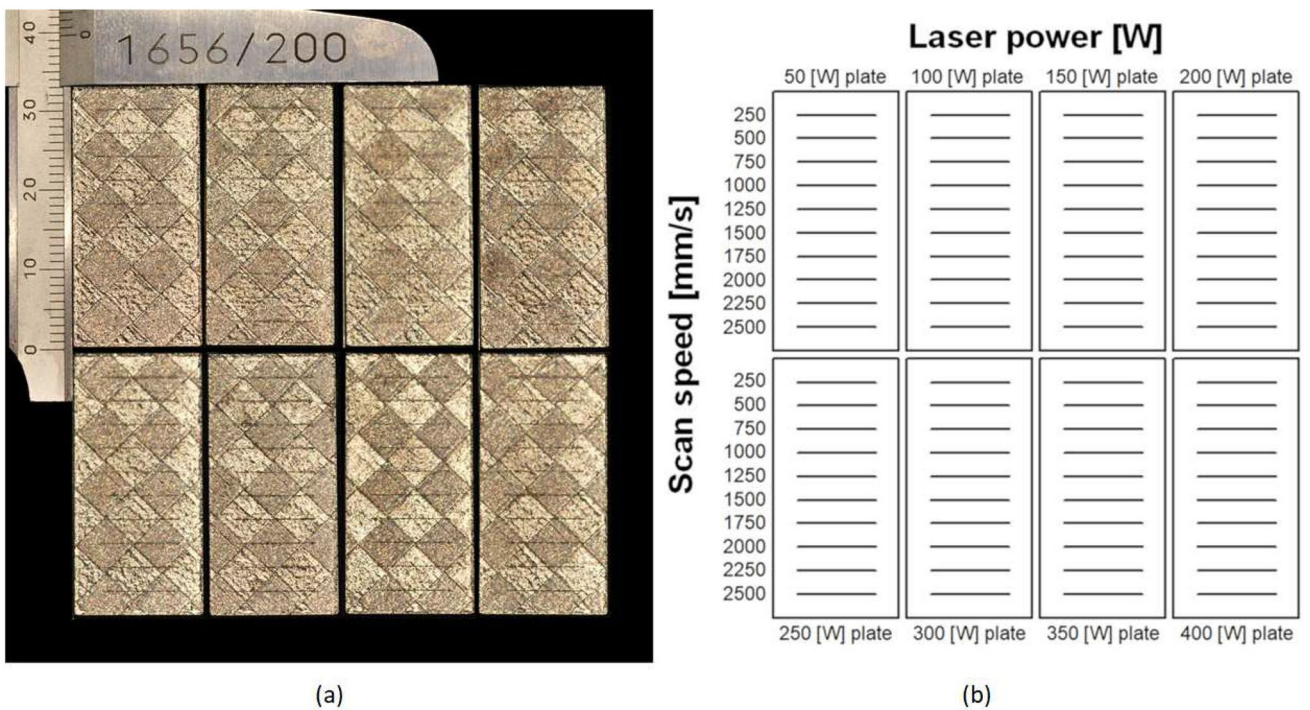


Fig. 6 Single tracks produced for the experiment and corresponding design of experiment. **a** Picture of the first replicate of specimens and **b** scheme of the adopted Design of Experiments

from keyhole to conduction mode. However, the transition range is typically tight and in this work it is comparable to the resolution of the experimental design.

Results are summarized in Fig. 7, where empty circles stand for specimens affected by pores, and full circles stand for specimens where pores were not found.

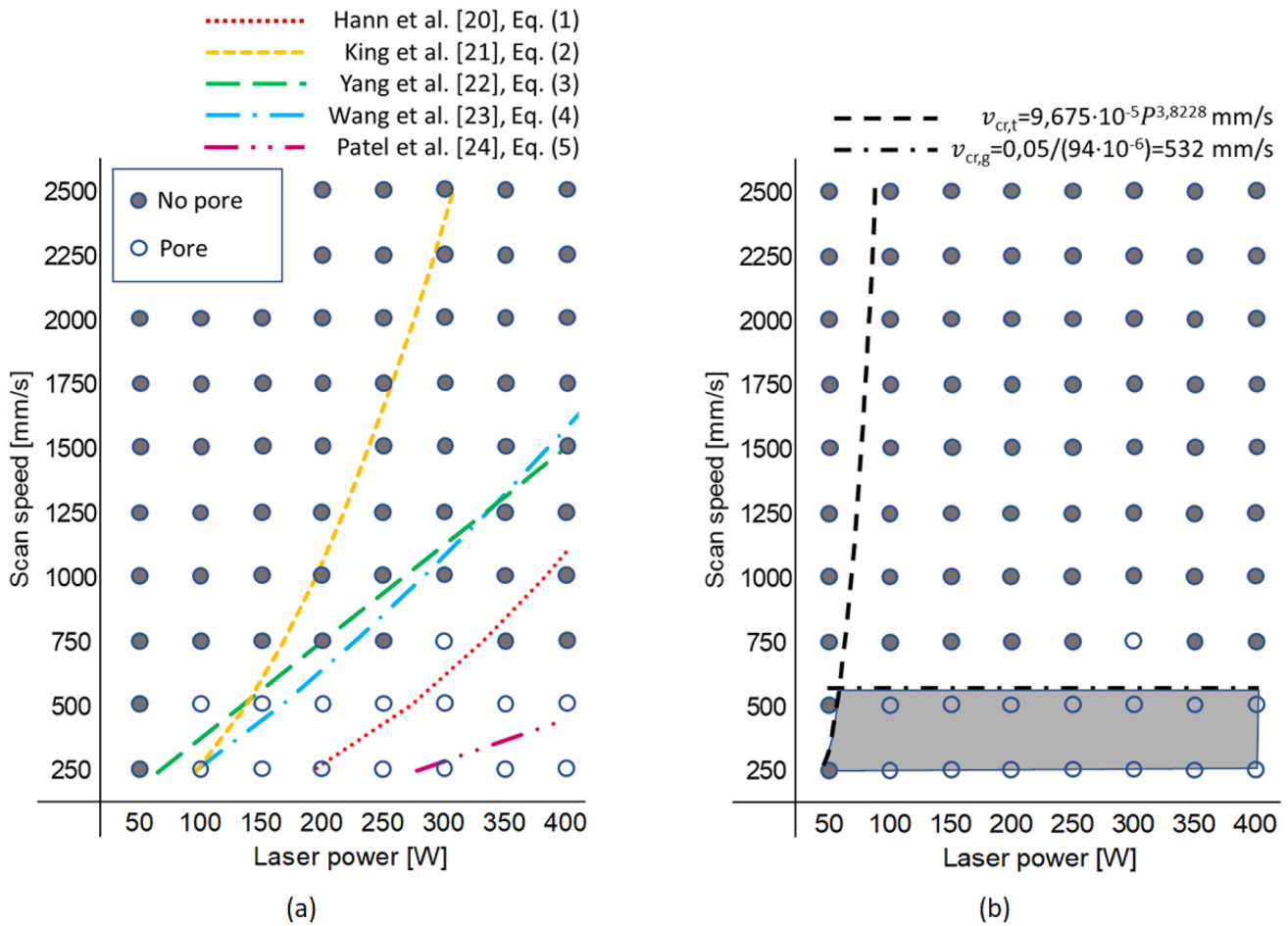


Fig. 7 a Keyhole prediction using conventional analytical models and b keyhole prediction obtained through the new model

Tracks cross sections illustrating the different types of melt-pool (and cavity) shapes, and the absence or presence of keyhole-induced porosity are shown in Fig. 8.

In Fig. 7, a conventional analytical models are applied on the experimental data. To this aim, Eqs. (1), (2), (3), (4) and (5) were plotted on the $P - v$ plane using the physical properties of the Ti6Al4V alloy, and by imposing $d_s = 50 \mu\text{m}$ and $t_l = 25 \mu\text{m}$. When required, h_d was quantified from the tracks width reported in [35] by assuming an overlap of 20%. It is clearly visible that their predictions were not accurate. Indeed, since they are mostly based on thermodynamics, they consist of inaccurate and monotonously increasing curves which fail to model the geometrical evolution of the keyhole cavity in the medium-high scanning speed range. On the one hand, this may result in the acceptance of inadequate process parameters. On the other hand, the most conservative models tend to exclude parameter combinations which are suitable for manufacturing fully dense 3D products. Although a poor surface finishing can be expected at some of the excluded

parameters combinations, they can be useful for increasing productivity when processing the product core [36].

The prediction provided by the new model is shown in Fig. 7b, where the black curves represent the two conditions that must be simultaneously met for the keyhole regime to occur. The first condition refers to the critical laser-material interaction time $t_{cr,t}$ having a purely thermodynamic meaning and resulting in a monotonously increasing curve similar to those of the other models. However, this threshold only concerns the low scanning speed region, where it provides a significantly more accurate prediction compared to all state of the art models.

The second condition refers to the closing time t_{clo} that is dependent on other important physical and geometrical factors. Actually, the condition

$$v_{cr,g} = \frac{d_s}{t_{clo}} \approx \frac{50 \mu\text{m}}{0.096 \text{ ms}} = 521 \frac{\text{mm}}{\text{s}} \tag{16}$$

is in perfect agreement with the experimental findings. It is important to notice that the closing time of Eq. 16 has been

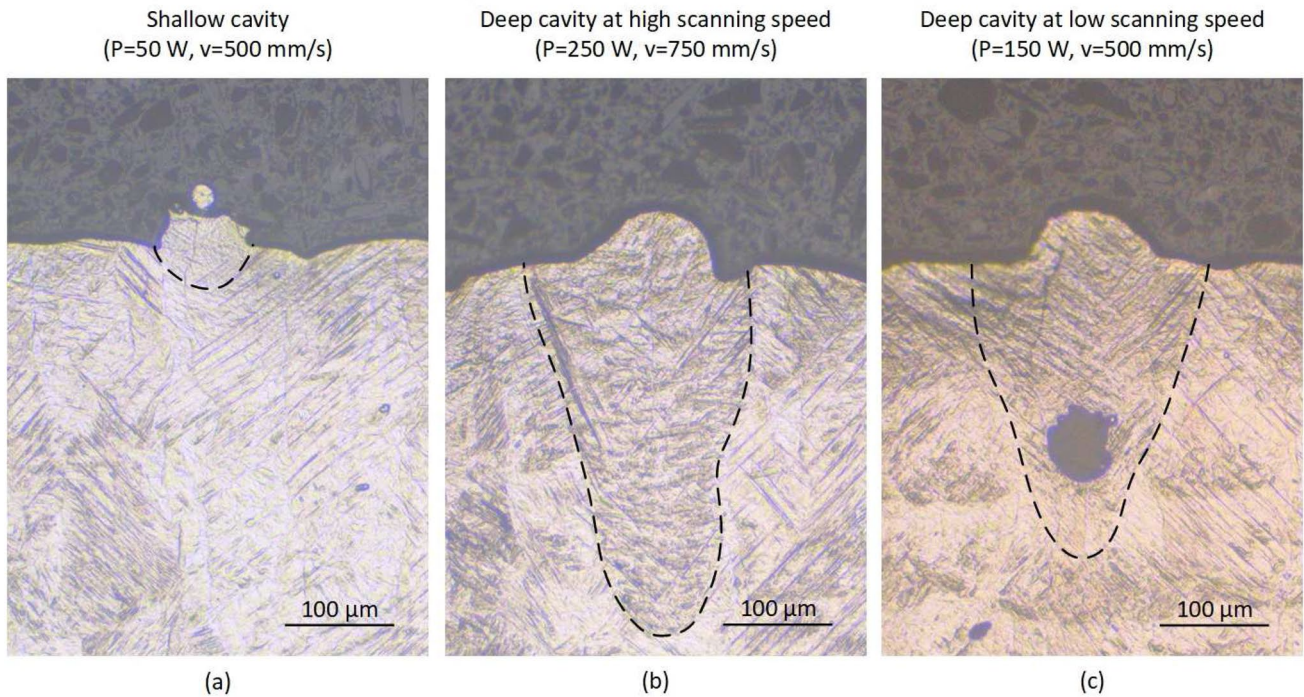


Fig. 8 Tracks cross sections illustrating the different types of process outputs observed: **a** shallow cavity due to short interaction time $t_{cr,t}$, **b** pore-free deep cavity at high scanning speed and **c** pore-affected

deep cavity at low scanning speed. Note that the pore-free cavity (**b**) is even deeper than the pore-affect one (**c**)

just estimated in subsection 3.2 from [26], where considerably larger laser beam diameters were adopted.

The intersection of the areas defined by the two curves—light gray region in Fig. 7b identifies the undesired process window where keyhole is very likely to arise. As it can be seen, it is in very good accordance with the experimental data. More specifically, the ratio of keyhole-free conditions that were wrongly classified as keyhole-affected conditions is 1.5% for the developed model, while it is between 0% and 43% for the conventional models. At the same time, the ratio of keyhole-affected conditions that were wrongly classified as keyhole-free conditions is 7% for the developed model, while it is between 7% and 47% for the conventional models. The general model performance was evaluated by computing its balanced accuracy, which can be expressed as follows:

$$A_{bal} = \frac{1}{2} \left(\frac{N_{kk}}{N_{k,tot}} + \frac{N_{ff}}{N_{f,tot}} \right) \quad (17)$$

where

- $N_{k,tot}$ is the total number of experimental conditions affected by keyhole porosities;
- N_{kk} is the number of cases affected by keyhole porosities that are correctly classified by a given model;

- $N_{f,tot}$ is the total number of keyhole-free experimental conditions;
- N_{ff} is the number of keyhole-free cases that are correctly classified by a given model.

According to this formula, the accuracy of the presented model is 96%, which is significantly higher than that of other state of the art models (Table 4).

Table 4 Balanced accuracy (Eq. 17) of the available models for the keyhole porosity prediction

Ref.	N_{kk}	N_{ff}	$N_{k,tot}$	$N_{f,tot}$	$A_{bal}(\%)$
[20]	8	62	15	65	74
[21]	14	37	15	65	75
[22]	14	57	15	65	90
[23]	13	56	15	65	86
[24]	3	65	15	65	60
This work	14	64	15	65	96

5 Conclusions

In this work, a physics-based semi-analytical method aimed at predicting the formation of keyhole-related porosity was developed. To this aim, the keyhole phenomenology was first reconstructed through a comprehensive literature review. It was found that the scanning speed v plays a central role in the considered phenomenon since at relatively high levels it inhibits the formation of humps and cause the keyhole front wall to tilt forward, thus resulting in a deflected vapor plume. This further leads to an elongated and stable cavity less prone to collapse. The extensive examination of the literature also showed that all the analytical models developed so far are purely thermodynamic, so they are unable to capture this important aspect. As a consequence, they may be highly inaccurate and not suitable for industrial applications.

Actually, it was proved that the keyhole porosity can be accurately predicted by requiring the accomplishment of two conditions, namely that the keyhole cavity is both deep and short at the same time. This implies that the scanning speed v is concurrently small enough to make the interaction time between laser and matter greater than a critical time that triggers the abrupt increase of the laser penetration rate inside the solid substrate, and lower than the speed at which the molten metal can fill the keyhole cavity. It was shown that the scanning speed threshold imposed by the first condition can be analytically expressed as an exponential function of the laser power and spot diameter, while the scanning speed threshold imposed by the second condition can be assumed proportional to the laser spot diameter d_s by means of a proportionality constant B that is only dependent on the processed material.

The developed model was tested on original experimental data presented by the authors in a previous data article [35], that were further extended by performing a second replicate to enhance the reliability of the results. When compared to the experimental data state of the art models were found too inclusive in the low scanning speed regime and too conservative in the medium scanning speed regime, thus excluding some promising process parameters combinations. On the contrary, the proposed model did perfectly recognize almost all the conditions affected by keyhole pores. At the same time, it correctly classified as keyhole-free almost all the process parameters combinations that were effectively free from this problem, thus avoiding an incorrect rejection of possibly good operating conditions. Some of the latter conditions may be suitable for increasing productivity when scanning the inner core of parts or in general non-demanding products in terms of surface finishing.

The new model was capable of correctly predicting the absence or occurrence of keyhole porosity in 96% of cases,

whereas the state of the art model achieved 60 ÷ 90% of balanced classification accuracy, when assessing the considered case study.

In the future it would be of further interest to validate the proposed model on other experimental datasets. Furthermore, it is believed that the unknown model coefficients derived here from experimental data could be analytically predicted or numerically computed from the material and laser properties and by modeling their reciprocal dynamic interaction. This may eliminate the experimental calibration phase of the model, thus further promoting its practical application.

Acknowledgements The Laboratory for Advanced Mechatronics - LAMA FVG - of the University of Udine is gratefully acknowledged for technical support. LAMA FVG is an international research center for product and process innovation where the three universities of Friuli Venezia Giulia (Italy) cooperate for promoting R & D activities at academic and industrial level. The authors are also grateful to M. Magnan for the examination of the experimental samples.

Author contributions EV: conceptualization, methodology, formal analysis, investigation, visualization, writing—original draft preparation, writing—review and editing. GT: validation, formal analysis, visualization, writing—review and editing. AL: validation, data acquisition, investigation, writing—review and editing. LF: validation, writing—review and editing, resource, supervision. MS: validation, visualization, writing—review and editing, resource, supervision.

Funding Open access funding provided by Università degli Studi di Udine within the CRUI-CARE Agreement. The authors declare that no funds, grants, or other support were received during the preparation of this manuscript.

Availability of data and materials All data analyzed during this study are available online.

Code availability Not applicable.

Declarations

Conflict of interest The authors have no conflicts of interest to declare.

Financial interests The authors declare they have no financial interests.

Non-financial interests The authors declare they have no non-financial interests.

Ethical approval Not applicable.

Research involving Human Participants and/or Animals Not applicable. The article involves no studies on humans.

Informed consent Not applicable.

Open Access This article is licensed under a Creative Commons Attribution 4.0 International License, which permits use, sharing, adaptation, distribution and reproduction in any medium or format, as long as you give appropriate credit to the original author(s) and the source, provide a link to the Creative Commons licence, and indicate if changes were made. The images or other third party material in this article are included in the article's Creative Commons licence, unless indicated

otherwise in a credit line to the material. If material is not included in the article's Creative Commons licence and your intended use is not permitted by statutory regulation or exceeds the permitted use, you will need to obtain permission directly from the copyright holder. To view a copy of this licence, visit <http://creativecommons.org/licenses/by/4.0/>.

References

- Grasso M, Colosimo BM (2017) Process defects and in situ monitoring methods in metal powder bed fusion: a review. *Meas Sci Technol* 28:044005. <https://doi.org/10.1088/1361-6501/aa5c4f>
- Gong H, Rafi K, Gu H, Ram GJ, Starr T, Stucker B (2015) Influence of defects on mechanical properties of Ti-6Al-4V components produced by selective laser melting and electron beam melting. *Mater Des* 86:545–554. <https://doi.org/10.1016/j.matdes.2015.07.147>
- DebRoy T, Wei HL, Zuback JS, Mukherjee T, Elmer JW, Milewski JO, Beese AM, Wilson-Heid A, De A, Zhang W (2018) Additive manufacturing of metallic components—process, structure and properties. *Prog Mater Sci* 92:112–224. <https://doi.org/10.1016/j.pmatsci.2017.10.001>
- Hojjatzadeh SMH, Parab ND, Guo Q, Qu M, Xiong L, Zhao C, Escano LI, Fezzaa K, Everhart W, Sun T, Chen L (2020) Direct observation of pore formation mechanisms during LPBF additive manufacturing process and high energy density laser welding. *Int J Mach Tools Manuf* 153:103555. <https://doi.org/10.1016/j.ijmactools.2020.103555>
- Liverani E, Fortunato A (2021) Additive manufacturing of AISI 420 stainless steel: process validation, defect analysis and mechanical characterization in different process and post-process conditions. *Int J Adv Manuf Technol* 117:809–821. <https://doi.org/10.1007/s00170-021-07639-6>
- Ki H, Mazumder J, Mohanty PS (2002) Modeling of laser keyhole welding: part I. Mathematical modeling, numerical methodology, role of recoil pressure, multiple reflections, and free surface evolution. *Metall Mater Trans A* 33:1817–1830. <https://doi.org/10.1007/s11661-002-0190-6>
- Ki H, Mazumder J, Mohanty PS (2002) Modeling of laser keyhole welding: part II. Simulation of keyhole evolution, velocity, temperature profile, and experimental verification. *Metall Mater Trans A* 33:1831–1842. <https://doi.org/10.1007/s11661-002-0191-5>
- Yuan W, Chen H, Cheng T, Wei Q (2020) Effects of laser scanning speeds on different states of the molten pool during selective laser melting: simulation and experiment. *Mater Des* 189:108542. <https://doi.org/10.1016/j.matdes.2020.108542>
- Cho JH, Na SJ (2006) Implementation of real-time multiple reflection and Fresnel absorption of laser beam in keyhole. *J Phys D Appl Phys* 39:5372. <https://doi.org/10.1088/0022-3727/39/24/039>
- Chen Y, Clark SJ, Leung CLA, Sinclair L, Marussi S, Olbinado MP, Boller E, Rack A, Todd I, Lee PD (2020) In-situ Synchrotron imaging of keyhole mode multi-layer laser powder bed fusion additive manufacturing. *Appl Mater Today* 20:100650. <https://doi.org/10.1016/j.apmt.2020.100650>
- Lee JY, Ko SH, Farson DF, Yoo CD (2002) Mechanism of keyhole formation and stability in stationary laser welding. *J Phys D Appl Phys* 35:1570. <https://doi.org/10.1088/0022-3727/35/13/320>
- Fabbro R (2010) Melt pool and keyhole behaviour analysis for deep penetration laser welding. *J Phys D Appl Phys* 43:445501. <https://doi.org/10.1088/0022-3727/43/44/445501>
- Lin R, Wang HP, Lu F, Solomon J, Carlson BE (2017) Numerical study of keyhole dynamics and keyhole-induced porosity formation in remote laser welding of Al alloys. *Int J Heat Mass Transf* 108:244–256. <https://doi.org/10.1016/j.ijheatmasstransfer.2016.12.019>
- Huang L, Hua X, Wu D, Ye Y (2019) Role of welding speed on keyhole-induced porosity formation based on experimental and numerical study in fiber laser welding of Al alloy. *Int J Adv Manuf Technol* 103:913–925. <https://doi.org/10.1007/s00170-019-03502-x>
- Miyagi M, Wang J (2020) Keyhole dynamics and morphology visualized by in-situ X-ray imaging in laser melting of austenitic stainless steel. *J Mater Process Technol* 282:116673. <https://doi.org/10.1016/j.jmatprotec.2020.116673>
- Tenbrock C, Fischer FG, Wissenbach K, Schleifenbaum JH, Wagenblast P, Meiners W, Wagner J (2020) Influence of keyhole and conduction mode melting for top-hat shaped beam profiles in laser powder bed fusion. *J Mater Process Technol* 278:116514. <https://doi.org/10.1016/j.jmatprotec.2019.116514>
- Shrestha S, Starr T, Chou K (2019) A study of keyhole porosity in selective laser melting: single-track scanning with micro-CT analysis. *J Manuf Sci Eng* 141:071004. <https://doi.org/10.1115/1.4043622>
- Bertoli US, Wolfer AJ, Matthews MJ, Delplanque JPR, Schoenung JM (2017) On the limitations of volumetric energy density as a design parameter for selective laser melting. *Mater Des* 113:331–340. <https://doi.org/10.1016/j.matdes.2016.10.037>
- Ferro P, Meneghello R, Savio G, Berto F (2020) A modified volumetric energy density-based approach for porosity assessment in additive manufacturing process design. *Int J Adv Manuf Technol* 110:1911–1921. <https://doi.org/10.1007/s00170-020-05949-9>
- Hann DB, Iammi J, Folkes J (2011) A simple methodology for predicting laser-weld properties from material and laser parameters. *J Phys D Appl Phys* 44:445401. <https://doi.org/10.1088/0022-3727/44/44/445401>
- King WE, Barth HD, Castillo VM, Gallegos GF, Gibbs JW, Hahn DE, Kamath C, Rubenchik AM (2014) Observation of keyhole-mode laser melting in laser powder-bed fusion additive manufacturing. *J Mater Process Technol* 214:2915–2925. <https://doi.org/10.1016/j.jmatprotec.2014.06.005>
- Yang J, Han J, Yu H, Yin J, Gao M, Wang Z, Zeng X (2016) Role of molten pool mode on formability, microstructure and mechanical properties of selective laser melted Ti-6Al-4V alloy. *Mater Des* 110:558–570. <https://doi.org/10.1016/j.matdes.2016.08.036>
- Wang Z, Liu M (2019) Dimensionless analysis on selective laser melting to predict porosity and track morphology. *J Mater Process Technol* 273:116238. <https://doi.org/10.1016/j.jmatprotec.2019.05.019>
- Patel S, Vlasea M (2020) Melting modes in laser powder bed fusion. *Materialia* 9:100591. <https://doi.org/10.1016/j.mtla.2020.100591>
- Pastor M, Zhao H, DebRoy T (2001) Pore formation during continuous wave Nd: YAG laser welding of aluminium for automotive applications. *Weld Int* 15:275–281. <https://doi.org/10.1080/09507110109549355>
- Cunningham R, Zhao C, Parab N, Kantzos C, Pauza J, Fezzaa K, Sun T, Rollett AD (2019) Keyhole threshold and morphology in laser melting revealed by ultrahigh-speed x-ray imaging. *Science* 363:849–852. <https://doi.org/10.1126/science.aav4687>
- Fabbro R, Chouf K (2000) Keyhole modeling during laser welding. *J Appl Phys* 87:4075–4083. <https://doi.org/10.1063/1.373033>
- Fabbro R, Chouf K (2000) Dynamical description of the keyhole in deep penetration laser welding. *J Laser Appl* 12:142–148. <https://doi.org/10.2351/1.521924>
- Matsunawa A, Kim JD, Seto N, Mizutani M, Katayama S (1998) Dynamics of keyhole and molten pool in laser welding. *J Laser Appl* 10:247–254. <https://doi.org/10.2351/1.521858>

30. Matsunawa A, Semak V (1997) The simulation of front keyhole wall dynamics during laser welding. *J Phys D Appl Phys* 30:798. <https://doi.org/10.1088/0022-3727/30/5/013>
31. Teng C, Pal D, Gong H, Zeng K, Briggs K, Patil N, Stucker B (2017) A review of defect modeling in laser material processing. *Addit Manuf* 14:137–147. <https://doi.org/10.1016/j.addma.2016.10.009>
32. Khairallah SA, Anderson AT, Rubenchik A, King WE (2016) Laser powder-bed fusion additive manufacturing: Physics of complex melt flow and formation mechanisms of pores, spatter, and denudation zones. *Acta Mater* 108:36–45. <https://doi.org/10.1016/j.actamat.2016.02.014>
33. Ready JF (1997) *Industrial applications of lasers*, 2nd edn. Elsevier, New York. <https://doi.org/10.1016/B978-0-12-583961-7.X5000-5>
34. Schneider M, Berthe L, Fabbro R, Muller M (2008) Measurement of laser absorptivity for operating parameters characteristic of laser drilling regime. *J Phys D Appl Phys* 41:155502. <https://doi.org/10.1088/0022-3727/41/15/155502>
35. Vaglio E, De Monte T, Lanzutti A, Totis G, Sortino M, Fedrizzi L (2020) Single tracks data obtained by selective laser melting of Ti6Al4V with a small laser spot diameter. *Data Brief* 33:106443. <https://doi.org/10.1016/j.dib.2020.106443>
36. Wang H, Zou Y (2019) Microscale interaction between laser and metal powder in powder-bed additive manufacturing: conduction mode versus keyhole mode. *Int J Heat Mass Transf* 142:118473. <https://doi.org/10.1016/j.ijheatmasstransfer.2019.118473>

Publisher's Note Springer Nature remains neutral with regard to jurisdictional claims in published maps and institutional affiliations.